nature communications

Article

https://doi.org/10.1038/s41467-025-57998-x

Upcycling polyolefins to methane-free liquid fuel by a Ru_1-ZrO_2 catalyst

Received: 26 September 2024

Accepted: 7 March 2025

Jicong Yan[1,9], Guanna Li[2,9], Zhanwu Lei[3,9], Xiaolu Yuan[1], Junting Li[1], Xiaoru Wang[1], Bo Wang[1], Fuping Tian[4], Tao Hu[4], Lei Huang[5], Yujia Ding[6], Xiaoke Xi[3], Feng Zhu[7], Shuo Zhang[8], Jiong Li[8], Yu Chen[8], Ruiguo Cao[3] & Xiang Wang[1]

Upcycling waste plastics into liquid fuels presents significant potential for advancing the circular economy but is hindered by poor selectivity and low-value methane byproduct formation. In this work, we report that atomic Ru-doped ZrO_2 can selectively convert 100 grams of post-consumer polyethylene and polypropylene, yielding 85 mL of liquid in a solvent-free hydrocracking. The liquid (C_5-C_{20}) comprises ~70% jet-fuel-ranged branched hydrocarbons (C_8-C_{16}), while the gas product is liquefied-petroleum-gas (C_3-C_6) without methane and ethane. We found that the atomic Ru dopant in the Ru-O-Zr moiety functionalizes its neighboring O atom, originally inert, to create a Brønsted acid site. This Brønsted acid site, rather than the atomic Ru dopant itself, selectively governs the internal C−C bond cleavage in polyolefins through a carbonium ion mechanism, thereby enhancing the yield of jet-fuel-ranged hydrocarbons and suppressing methane formation. This oxide modulation strategy provides a paradigm shift in catalyst design for hydrocracking waste plastics and holds potential for a broad spectrum of applications.

Polyolefins (PO), comprising two-thirds of total plastic production[1], are the most widely used plastics due to their inherent durability and resistance to degradation. However, these traits also contribute to the persistence of PO waste in the environment, causing severe environmental issues and a loss of 95% economic value of plastic[2]. PO waste, primarily sourced from fossil feedstock, represents a large reservoir of carbon and hydrogen, offering great opportunities for a circular economy through upcycling processes[3–6]. Chemical upcycling can tackle this challenge[7] by deconstructing PO into valuable chemicals[8,9] and sustainable fuels[10–18], thus enhancing the value chain of plastic waste recycling and creating a circular plastic economy.

Converting waste PO to liquid fuels presents a high potential to partially replace petroleum-route fuels and reduce global net carbon emissions. Common chemical upcycling strategies in practical terms include gasification and pyrolysis[14,15], but these methods are energy-intensive, produce broad product distributions, and yield significant amounts of low-value methane. In contrast, hydrocracking with metal/oxide bifunctional catalysts has shown promise in producing high-value fuels, waxes, and lubricants under milder conditions, usually below 300 °C[16–24]. Nevertheless, achieving high selectivity for liquid fuels, particularly in the jet fuel range (C_8-C_{16}), over metal/oxide catalysts remains challenging.

---

[1]State Key Laboratory of Fine Chemicals, School of Chemical Engineering, Dalian University of Technology, Dalian, Liaoning, China. [2]Biobased Chemistry and Technology, Wageningen University, WG Wageningen, the Netherlands. [3]Department of Materials Science and Engineering, University of Science and Technology of China, Hefei, Anhui, China. [4]School of Chemistry, Dalian University of Technology, Dalian, Liaoning, China. [5]Research Center of Nano Science and Technology, College of Sciences, Shanghai University, Shanghai, China. [6]Department of Physics and CSRRI, Illinois Institute of Technology, Chicago IL, USA. [7]TRACE EM Unit and Department of Materials Science and Engineering, City University of Hong Kong, Kowloon, Hong Kong SAR, China. [8]Shanghai Synchrotron Radiation Facility, Shanghai Advanced Research Institute, Chinese Academy of Sciences, Shanghai, China. [9]These authors contributed equally: Jicong Yan, Guanna Li, Zhanwu Lei. e-mail: xiangwang@dlut.edu.cn

Among metal/oxide catalysts, Ru-based catalysts have been studied in the hydroconversion of polyolefins due to their outstanding efficiency in breaking C−C bonds[25]. However, its tendency to generate substantial amounts of low-value methane significantly diminishes the economic viability of the hydrocracking process. Several operating strategies have been developed to suppress methane formation, such as decreasing reaction temperature[26], shortening reaction time, and increasing H_2 pressure[27,28]. However, these operating optimizations often result in the under-cracking of polyolefins, leading to a broad carbon distribution with low selectivity for jet-fuel-ranged hydrocarbons. To overcome the economic bundle by maximizing jet fuel component yield and minimizing methane production, the fundamental solution still lies in designing an active site capable of selectively breaking the internal C−C bond of PO rather than the terminal C−C bond. Efforts have been focused on the manipulation of supported metal species[17], and regulation of the oxidation state[29,30], particle size[21,31–34] and surface decoration[35] of these metal species has proved its effectiveness in reducing undesired methane production. For instance, positively charged Ru species have been reported to favor the cleavage of the internal C−C bond over the terminal C−C bond, thus inhibiting methane formation, but the yield of methane is still at 4.5% with a conversion of PE at 80%[36]. Ru nanoparticles with multiple exposed Ru sites tend to cleave the terminal C−C bond producing methane, and the sub-nanometer particle or single atom of Ru was found effective in suppressing methane formation, but a low methane yield was only obtained in the scenario of under-cracking of PO with a wide distribution of the liquid/wax products up to C_{40}[31,32]. Decoration of 5 wt% Ru/ZrO_2 with 25 wt% WO_3 significantly reduced methane yield from 15% to 5%, but this improvement came at the cost of PO conversion reduced from 75% to 60%[35]. Therefore, the low methane output and the high jet fuel yield still cannot be simultaneously achieved at a high polyolefin conversion, appearing either under-cracking or over-cracking. Still, if the metal site governing the internal C−C bond cleavage is unclear, impeding the rational design of active sites that can selectively promote internal C-C scission while not triggering terminal cascades.

Instead of manipulating the supported metal species, herein, we functionalize the lattice oxygen of oxides via atomic doping to be the active site for selectively cleaving the internal C−C bond of polyolefins. In this proof-of-concept work, we chose ZrO_2, an originally inert oxide, as the base material, and Ru, a well-known methanation metal typically favoring methane formation during hydrocracking, as the dopant. We found that the Ru dopant turns its neighboring originally inert O atom of the Ru-O-Zr moiety into an active site for selectively cleaving the internal C-C bond. This Ru-doped ZrO_2 (Ru_1-ZrO_2) achieves ideal hydrocracking of 100 g of post-consumer PP and PE mixture in a solvent-free process, yielding 85 mL of liquid fuels with approximately 70% jet-fuel-range hydrocarbons, without forming low-value methane and ethane.

Results

Hydrocracking polyolefins

In a typical hydrocracking process involving 4 grams of PE or PP, a conversion of over 98% can be achieved using Ru_1-ZrO_2 at 250 °C under 3 MPa H_2 for 8 hours, yielding approximately 2.8 grams of liquid and 1.1 grams of gas, as illustrated in Fig. 1a. The products are in gas and liquid phases mainly ranging from C_3 to C_{20}, and remain consistent regardless of the substrate as PE or PP (Supplementary Fig. 1). The liquid consists of approximately 70% jet-fuel-range hydrocarbons (C_8-C_{16}), while the gas primarily comprises C_3-C_6 LPG-range hydrocarbons (liquified-petroleum-gas, C_3-$C_4 > 70\%$), and is almost free of methane and ethane (<0.007% and <0.068% mass yields, respectively, as shown in Supplementary Figs. 1, 2). Notably, for the gaseous C_4-C_6 fraction, *iso*-alkanes dominate with a 93% weight fraction (Supplementary Fig. 3), even when the substrate is the less branched PE. This result implies that significant isomerization occurs over Ru_1-ZrO_2 during hydrocracking.

High temperatures enhance the thermodynamic driving force toward terminal C−C bond cleavage, leading to increased methane production[26,37]. However, they also shorten the required reaction time, which is often practical in industrial settings. Low H_2 pressure is also highly desirable in real practice due to the lower equipment requirements, but it reduces competitive hydrogen adsorption on the catalyst resulting in higher methane formation rates[27,28,38]. Prolonged reaction times are often required for cracking the heavy hydrocarbons to get the liquid product, but it increases the likelihood of over-cracking lighter hydrocarbon products to methane. PP, which contains more methyl groups, tends to produce more methane than PE, due to terminal C−C bond cleavage[33,39]. To examine the product preference for jet-fuel-ranged hydrocarbons and resistance to methane formation, a proof test over Ru_1-ZrO_2 was conducted under conditions favorable for methane formation, i.e., PP as the substrate at 300 °C under H_2 of 1–4 MPa for 8 hours (note: 2 hours is sufficient to achieve 98% PP conversion under these conditions, as shown in Supplementary Fig. 4).

As shown in Supplementary Fig. 5, increasing the H_2 pressure from 1 MPa to 2 MPa enhances the PP conversion from 92% to nearly 100% and increases the liquid yield from 65 wt% to 72 wt%. Further increasing H_2 pressure from 2 MPa to 4 MPa hardly affects the conversion of PP or the yield of liquid. Nonetheless, higher H_2 pressure results in greater H_2 consumption (Supplementary Fig. 6), indicating that more C-C bonds are cleaved, producing short-chain hydrocarbons but they remain in the liquid phase. This is evidenced by the narrower carbon number distribution of the liquid as the H_2 pressure increases (Fig. 1b). Notably, although the carbon number distribution narrows to C_3-C_{18} with increased H_2 pressure, it remains centered around C_8, leading to an increased selectivity of jet-fuel-ranged hydrocarbons (C_8-C_{16}) up to 77% in the liquid, while maintaining liquid and gas yields at 75 wt% and 25 wt%, respectively. These results suggest that the over-cracking of lighter liquid hydrocarbons is suppressed, while the heavier hydrocarbons larger than C_8 are selectively deconstructed. As previously reported[26–28,37,38], the low H_2 pressure and high reaction temperatures favor the formation of methane and ethane. This trend holds true in this proof test (Supplementary Table 1 lists C_1-C_2 values from Fig. 1b). However, Ru_1-ZrO_2 still keeps the methane yield below 0.2 wt% while maintaining liquid fuels (C_5-C_{20}) around 70 wt%, even under the reaction condition most greatly favoring methane formation.

The influence of H_2 pressure on the composition of the liquid product is more pronounced than that on the gas product, as visually indicated by the color change of the liquid from orange to yellow to colorless with the increase of H_2 pressure from 1 MPa to 4 MPa (Fig. 1c). This observation motivated us to prioritized Ultraviolet-Visible (UV-Vis) absorption spectroscopy characterization for these liquid products. The absorption at 210–320 nm is present for all liquid products (Fig. 1d) but its intensity significantly decreases as the color of the liquid changes from orange to colorless. This adsorption can be attributed to the π-π^* transition of aromatics[40]. To further confirm the formation of aromatics, the ^{13}C–^{1}H HSQC NMR was employed. Besides the correlation peaks assigned to $-CH_3$, $-CH_2$, and -CH groups (as marked in Fig. 1e), the correlation peaks at (^1H: 2.0–2.5 ppm, ^{13}C: 15–20 ppm) are observed and resulted from CH_x- directly connected with aromatic rings. The presence of the signals at (^1H: 6.7–8.0 ppm, ^{13}C: 115–135 ppm)[8] attributed to aromatic rings also confirmed the presence of aromatics in the liquid product (Supplementary Fig. 7). The relative concentration of aromatics in the liquid product decreases as the H_2 pressure increases (Fig. 1f, plotted based on the calculation from Supplementary Fig. 8), which is consistent with the UV-Vis spectra results, indicating lower H_2 pressure facilitates the formation of aromatics. These findings not only reaffirm the absence of methane even under reaction conditions favoring terminal C-C bond cleavage but

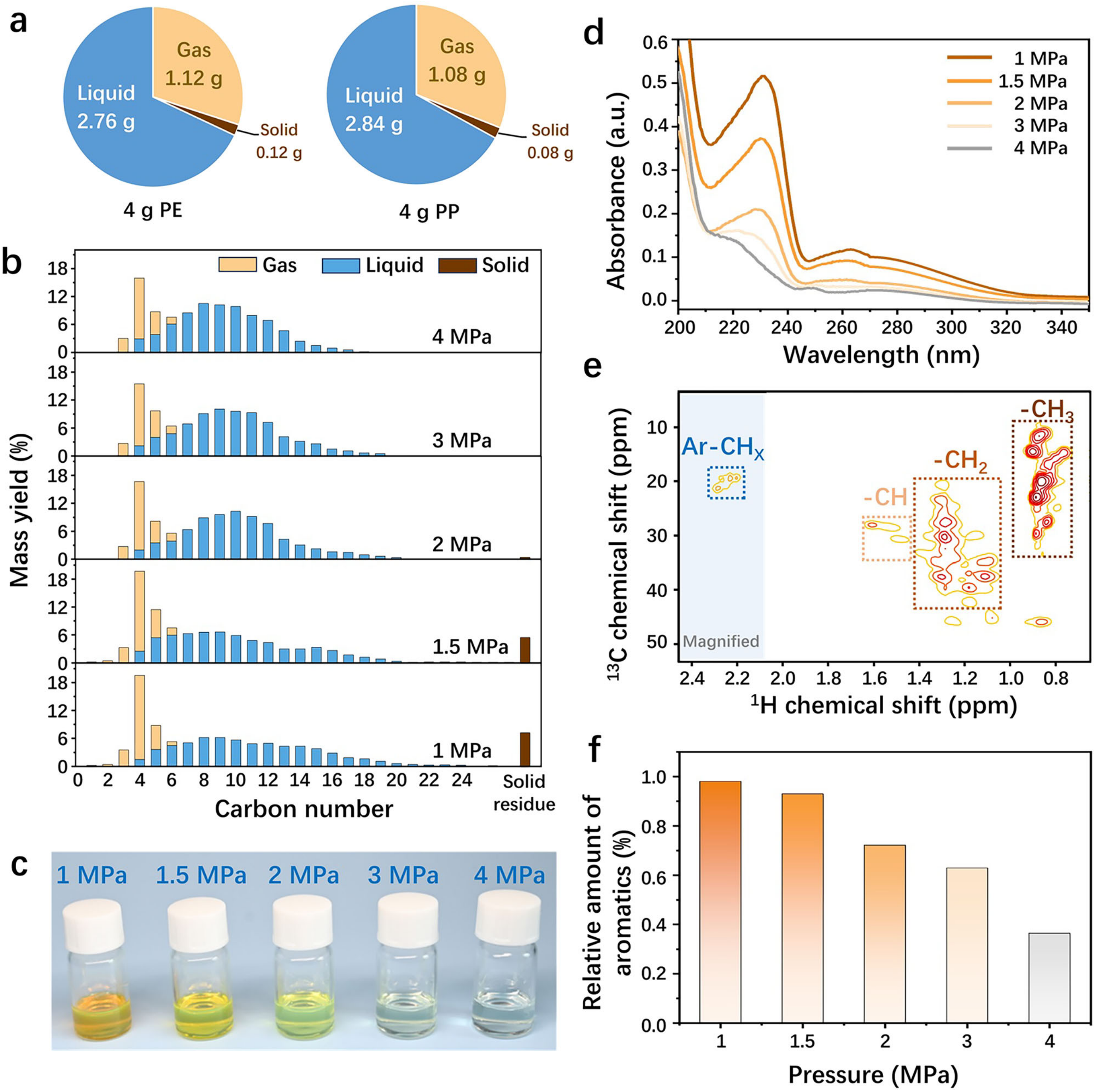

Fig. 1 | Solvent-free hydrocracking of PE and PP to methane-free fuels. a The yields of liquid and gaseous products in solvent-free hydrocracking 4 g PE or PP over Ru_1-ZrO_2 at 250 °C under 3 MPa H_2 for 8 hours. **b–f** Hydrocarbon distribution (**b**), Photo (**c**), UV- Vis absorption spectra (**d**), ^{13}C–^1H HSQC NMR (**e**) and relative amount of aromatics (**f**) calculated based on ^1H NMR (Supplementary Fig. 8) of the liquid product of hydrocracking PP on Ru_1-ZrO_2 at 300 °C under 1.5 MPa H_2 (**e**) and 1-4 MPa H_2 (**f**) for 8 hours.

also indicate the occurrence of dehydrogenation and isomerization during the hydrocracking reactions.

Identification of active site

This as-prepared Ru_1-ZrO_2 with 1.3 wt% Ru loading exhibits a tetragonal phase of ZrO_2 with no diffraction peaks attributed to Ru in X-ray diffraction (XRD) patterns (Supplementary Fig. 9). The particle size of Ru_1-ZrO_2 is around 5 nm (Fig. 2a), and energy-dispersive X-ray spectroscopy (EDS) element mappings confirm that the absence of Ru clusters in the catalyst (Fig. 2b). The HAADF-STEM image shows bright atoms randomly doped in the lattice of ZrO_2 (Fig. 2c), presumed to be Ru. Fourier transform extended X-ray absorption fine structure (EXAFS) spectra display a major peak corresponding to the Ru-O scattering path at ~1.5 Å in the first coordination sphere (Fig. 2d). The first-shell Ru-O coordination number (CN) is determined to be four based on EXAFS fitting (Supplementary Table 2 and Supplementary Fig. 10). These results confirm that the Ru species in Ru_1-ZrO_2 is atomic Ru coordinated with four O atoms in the ZrO_2 lattice. This is further supported by X-ray absorption near edge structure (XANES) and X-ray photoelectron spectroscopy (XPS) results (Fig. 2e and Supplementary Fig. 11), indicating that the Ru species in Ru_1-ZrO_2 are in an oxidized state rather than a metallic state.

Temperature-programmed reduction with H_2 (H_2-TPR) was conducted to understand the impact of the interaction between ZrO_2 and Ru on the reduction of the Ru and ZrO_2 components in the catalyst. Supported 1.5 wt% Ru/ZrO_2, 1.6 wt% Ru/SiO_2 and as-prepared bare ZrO_2 were used as references. To obtain the full TPR profiles in the range of 100–800 °C, none of these samples were pretreated in H_2, ensuring that

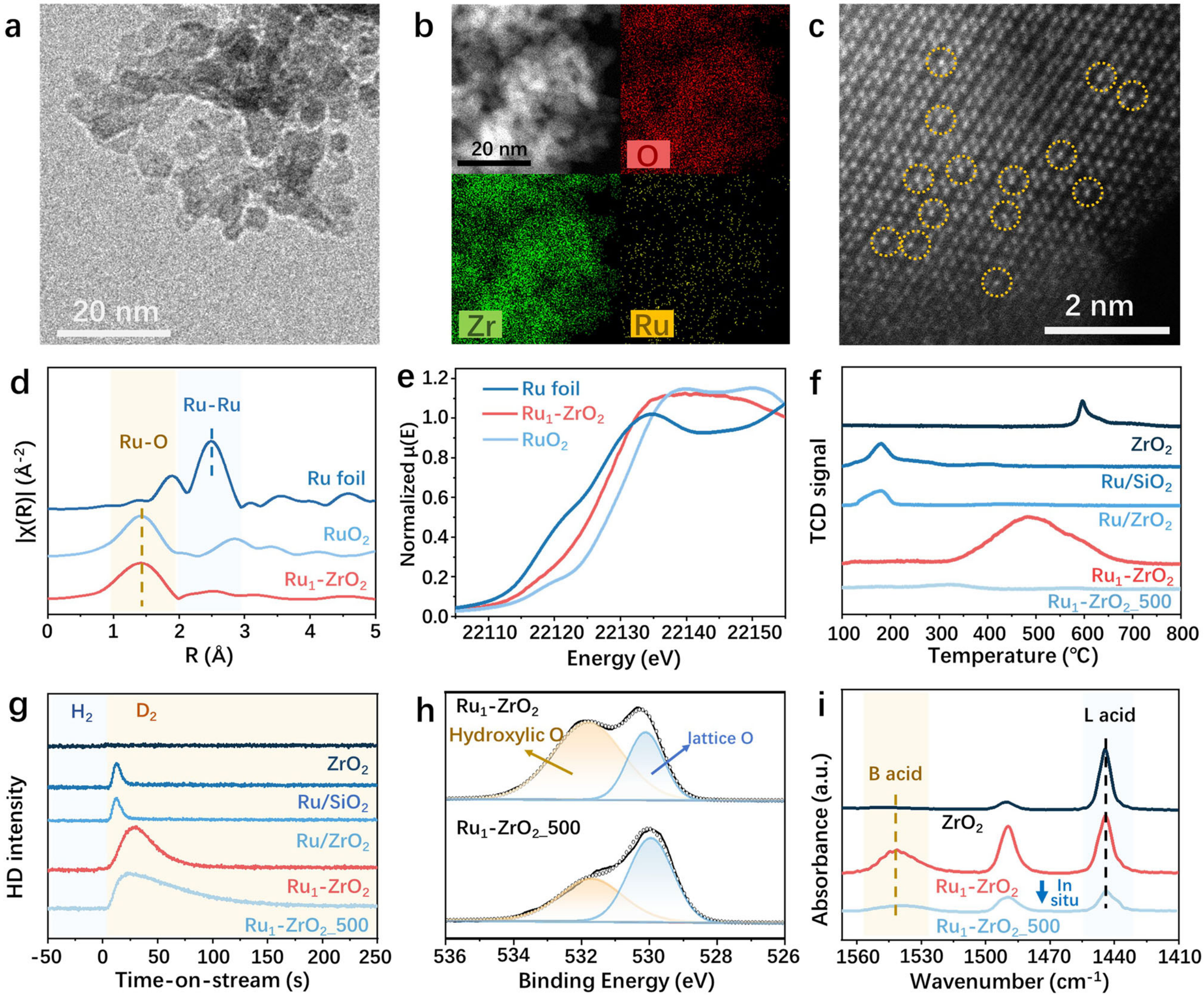

Fig. 2 | Relationship of Ru-O-Zr structure and performance of Ru_1-ZrO_2. **a**–**e** TEM image (**a**), EDS element mappings (**b**), HAADF-STEM image (**c**), Fourier transform of EXAFS spectra (**d**), and Ru *K*-edge XANES spectra (**e**) of Ru_1-ZrO_2. Ru foil and RuO_2 were used as references. **f** H_2-TPR profiles of ZrO_2, Ru/SiO_2, Ru/ZrO_2, Ru_1-ZrO_2, and Ru_1-ZrO_2_500. These samples were not pretreated in H_2 at 275 °C to obtain their complete TPR profiles. **g** H_2/D_2 switch experiment tracking m/z = 3 (HD) by mass spectrometer: 10% H_2/Ar flow switched to 10% D_2/Ar flow with a constant rate of 20 mL/min at 250 °C at the time of 0 s. **h** O 1*s* XPS spectra of Ru_1-ZrO_2 and Ru_1-ZrO_2_500. **i** FTIR spectra of pyridine adsorption at room temperature on ZrO_2 and Ru_1-ZrO_2 before and after (Ru_1-ZrO_2_500) in situ treatment in 20% H_2/Ar at 500 °C.

Ru remained in the oxidized state at the start of the H_2-TPR measurement. A peak at 180 °C is observed for supported Ru/SiO_2 and Ru/ZrO_2 (Fig. 2f) and attributed to the reduction of RuO_2 clusters[39] to metallic Ru (confirmed by HRTEM in Supplementary Fig. 12). For as-prepared bare ZrO_2, a peak around 600 °C is observed and attributed to the reduction of ZrO_2[41]. Unlike these two peaks, a significant peak around 500 °C is observed for Ru_1-ZrO_2. The peak is much closer in temperature to the ZrO_2 reduction peak than to the RuO_2 reduction peak, but its integration intensity is much higher than that of ZrO_2 reduction peak. Quantitative analysis of these peaks indicates that the amount of H_2 consumed by Ru_1-ZrO_2 is around 12 times higher than that consumed by supported Ru/SiO_2, Ru/ZrO_2, and ZrO_2 (Supplementary Fig. 13). This result confirms the observation of HRTEM and EXAFS that no Ru clusters or nanoparticles are present in Ru_1-ZrO_2, and further indicates that the atomic Ru dopants render more O atoms in Ru_1-ZrO_2 reducible compared to as-prepared bare ZrO_2. Therefore, it is confirmed that all Ru atoms were doped into the crystal of ZrO_2, forming the moieties of Ru-O-Zr, where the O atoms were activated due to the doping of Ru.

None of the supported Ru/SiO_2, Ru/ZrO_2, and bare ZrO_2 references show activity in the hydrocracking of PP (Supplementary Fig. 14). The significant difference between the active Ru_1-ZrO_2 and the inert references, as reflected in TPR profiles, is the prominent peak at 500 °C. We speculated that this peak-related structure, i.e., Ru-O-Zr, is relevant to the catalytic performance of Ru_1-ZrO_2. To verify this correlation, the Ru-O-Zr species were intentionally demolished by treating the Ru_1-ZrO_2 at 500 °C in a 20% H_2/Ar flow of 50 mL/min for 0.5 hours (denoted as Ru_1-ZrO_2_500). We found that in Ru_1-ZrO_2_500, the disappearance of the Ru-O-Zr reduction signal in the H_2-TPR profile (Fig. 2f) is accompanied by the loss of activity in PP hydrocracking, as demonstrated by the weight-balanced post-reaction solid residue (Supplementary Fig. 15) and the unchanged pressure during the reaction (Supplementary Fig. 16).

We further pursued which atomic site within the Ru-O-Zr moiety governs the internal C-C bond cleavage, so the changes in the Ru_1-ZrO_2 after H_2 treatment at 500 °C were studied. It was found that Ru_1-ZrO_2_500 maintains the tetragonal phase of ZrO_2 (XRD in Supplementary Fig. 17), and Ru remains atomic dopant within the ZrO_2 crystal, as depicted by HRTEM (Supplementary Fig. 18) and EXAFS (Supplementary Fig. 19). However, XANES (Supplementary Fig. 20) and XPS (Supplementary Fig. 21) indicate that the oxidation states of both

Ru and Zr shift toward their reduced states after H_2 treatment. Inductively coupled plasma-optical emission spectroscopy (ICP-OES) and XPS analyses suggest no loss of Ru after this H_2 treatment (Supplementary Table 3). The capability of hydrogenation/dehydrogenation involving H_2 dissociation of the catalysts was further examined using an H_2/D_2 switch experiment. As shown in Fig. 2g, the integrated intensity of the HD peak on Ru_1-ZrO_2_500 is slightly higher than that on Ru_1-ZrO_2, but both of them are more than 8 times higher than that on supported Ru/SiO_2 and Ru/ZrO_2. This observation demonstrates that the hydrogenation/dehydrogenation capability of Ru_1-ZrO_2_500 is enhanced or at least maintained compared to Ru_1-ZrO_2. During this H_2 treatment, the significant change in the Ru-O-Zr moiety is the removal of its O atom, as evidenced by the formation of H_2O (H_2-TPR-MS in Supplementary Fig. 22) and the decreased intensity of hydroxylic O in O 1*s* XPS spectra[42,43] (Fig. 2h). Therefore, we conclude that within the Ru-O-Zr moiety, it is the O atom, rather than Ru, that is the key site governing C-C bond cleavage in polyolefin hydrocracking.

Given the observation of isomerization during the hydrocracking PO, the acid sites were further studied. Pyridine-FTIR spectra (Fig. 2i) show only Lewis acid sites with a feature peak at 1444 cm^{-1} on the inert ZrO_2[16]. Upon doping with atomic Ru, another peak at 1540 cm^{-1}, attributed to Brønsted acid sites[16], is observed on Ru_1-ZrO_2. After in situ treatment of Ru_1-ZrO_2 at 500 °C in 20% H_2/Ar (equivalent to Ru_1-ZrO_2_500), a significant decrease in the intensities of the FTIR peaks is observed, particularly for the peak attributed to Brønsted acid sites, indicating a dramatic decrease in the amount of acid sites. This result is further confirmed by the temperature-programmed NH_3 desorption (NH_3-TPD). The integrated intensity of NH_3 desorption peak for Ru_1-ZrO_2 is 11 times higher than that for Ru_1-ZrO_2_500 (Supplementary Fig. 23). Moreover, the temperature for the complete NH_3 desorption is observed up to 450 °C on Ru_1-ZrO_2, while it is only around 260 °C for Ru_1-ZrO_2_500. These results reveal a dramatic decrease in both the population and strength of the acid sites on Ru_1-ZrO_2 after H_2 treatment at 500 °C. Given that both the activated atom after atomic Ru doping and the removed atom after the H_2 treatment at 500 °C are the O atom of the Ru-O-Zr moiety, it is concluded that the O atom of the Ru-O-Zr moiety has a dangling H, which acts as the Brønsted acid site.

We further performed charge and chemical bonding analysis for Ru-O-Zr moiety with a dangling H on the Ru-doped ZrO_2. Crystal Orbital Hamilton Population (COHP) analysis (Supplementary Fig. 24) revealed that, compared to ZrOHZr (assuming it exists), the bonding and antibonding O-H interactions in RuOHZr shifted to higher energy levels. This indicates that the O-H interaction in RuOHZr is relatively weaker, suggesting higher acidity of the OH group. Moreover, the integrated COHP values (Supplementary Table 5) show that the O-H bond distance in the RuOHZr moiety is longer than ZrOHZr and is closer to the Fermi level, further suggesting a weaker O-H interaction, i.e. a stonger acidity, in RuOHZr, which is in line with the results of NH_3-TPD.

Mechanism of selective internal C-C bond cleavage

We performed the hydrocracking of *n*-octane, aiming to get a preliminary understanding of the way of PO hydrocracking on Ru_1-ZrO_2. The products from *n*-octane are also free of methane and ethane, predominated by *iso*-butane with a selectivity of 60% in the gas products (Supplementary Fig. 25a). This product distribution indicates that the isomerization followed by β-scission of the carbonium ion regime is the primary pathway in the hydrocracking of *n*-octane (details in Supplementary Fig. 25b). The methane-free branched products from the hydrocracking of longer-chain hydrocarbons (Supplementary Fig. 26), such as *n*-dodecane (C_{12}) and squalane (C_{30}), further verified this conclusion. With this understanding, we conducted density functional theory (DFT) calculations to explore why the products are free of methane and dominated by isomerized hydrocarbons during PP hydrocracking over Ru_1-ZrO_2.

During PP deconstruction, the formation of the more stable tertiary carbonium ion is favored over, primary and secondary carbonium ions[44–46]. For the production of lighter hydrocarbons, the tertiary carbonium ion forms at the terminal of the carbon chain either initially or as a result of precedent β-scission of an internal C-C bond (Fig. 3a). The β-scission triggered by the terminal tertiary carbonium ion (scissors-marked molecule in the left panel), forms one *i*-C_4 molecule and a long-chain hydrocarbon with a secondary carbonium ion. Subsequent depolymerization from the resulting secondary carbonium ion of the residue long-chain hydrocarbon can proceed through three options: 1) isomerization (blue route), 2) direct β-scission (green route), or 3) rearrangement to form a tertiary carbonium ion (orange route). Regarding route 1), after isomerization there are two plausible C-C bond cleavage sites (marked with grey and red scissors) via β-scission, forming methane and *i*-C_5, respectively. DFT calculations indicate that the reaction forming methane is energetically less favorable ($\Delta E = -0.28$ eV, $E_a = 2.84$ eV) than the other one forming *i*-C_5 ($\Delta E = -1.18$ eV, $E_a = 1.69$ eV). Similarly, route 3) also has two C-C cleavage options (marked with grey and red scissors) via β-scission, and the one leading to ethane formation is less dominant than the other one forming *i*-C_6. The reaction energy of β-scission to form propane is −0.82 eV in route 2), while it is an endothermic process to produce methane with a reaction energy of 1.20 eV.

Furthermore, reaction energy and transition state calculations (details in Supplementary Figs. 27, 28) demonstrated that route 1) isomerization (blue route) is kinetically and thermodynamically the most favorable pathway (primary pathway) among the three routes assessed. The prevalence of *i*-C_4 and *i*-C_5 as preferred gaseous products, stemming from route 1) indicated by DFT calculation, aligns well with the distribution of the gaseous species obtained from hydrocracking PP (Supplementary Fig. 3). In all pathways, the carbonium ion either succeeds and circularizes the hydrocracking loop to produce shorter-chain hydrocarbons or is terminated by a hydrogenation reaction.

The catalytic cycle of PO (PE or PP) hydrocracking on Ru_1-ZrO_2 is depicted in Fig. 3b. The PO is dehydrogenated on the atomic Ru site of the Ru-O-Zr moiety and then transferred to the Ru-neighboring O site, which is topped with a dangling H and functionalized as the C-C bond breaking site upon the doping of atomic Ru into ZrO_2. On the O site, a carbonium ion forms, followed by isomerization or rearrangement and subsequent β-scission of the internal C-C bond, which is the rate-determining step. This process forms two shorter-chain hydrocarbons, one of which contains a new carbonium ion. The in situ-generated carbonium ion either undergoes a hydrogenation reaction to desorb or repeats the cycle of isomerization and β-scission. H_2 dissociation competes with PO dehydrogenation over Ru and supplies surface H species for hydrogenation reaction or spillover to the Ru-neighboring O site for hydrocracking. This mechanism explains why PO dehydrogenation-induced aromatics formation is suppressed as H_2 pressure increases. The atomic metal (Ru) and acid site (O) in close proximity substantially reduce mass transfer between them, resulting in high efficiency and inhibition of the side reaction of hydrogenolysis to methane.

Practice

The robustness of Ru_1-ZrO_2 was assessed by the cycling experiment. No decrease in liquid yield, which is maintained at around 70 wt%, was observed after 6 cycles (Fig. 4a). HRTEM and EDS mapping (Supplementary Fig. 29) revealed Ru species do not undergo aggregation after the reaction. Furthermore, EXAFS and XANES (Supplementary Fig. 30) confirmed the catalyst's exceptional stability, with Ru remaining embedded as single atoms within the ZrO_2 lattice after the reaction. In real practice, the one-pot upcycling of 100 grams of mixed post-consumer PP and PE wastes, such as lunch boxes, soft drink cups, masks, bags, pipets, packing films, over Ru_1-ZrO_2 at 300 °C under

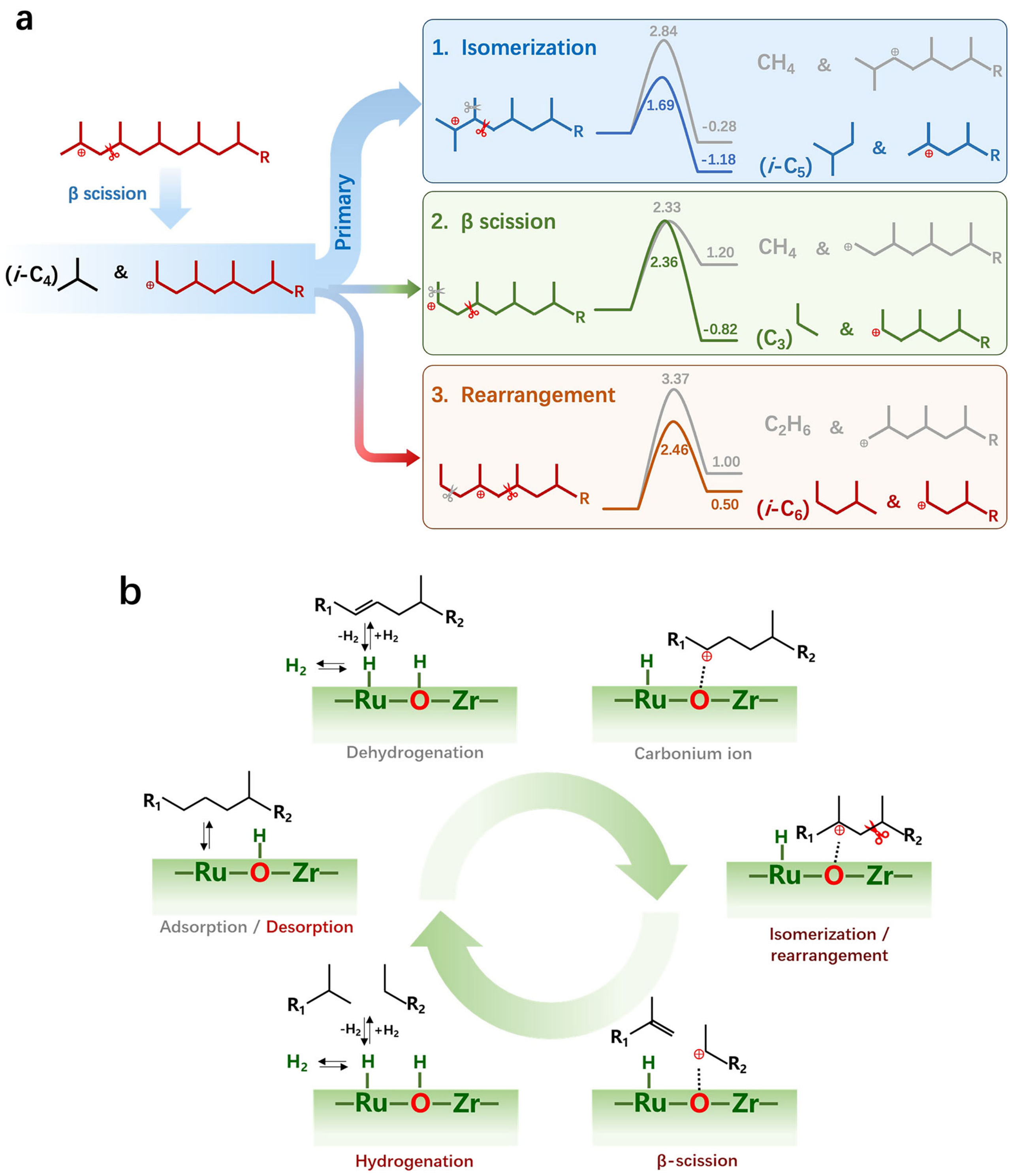

Fig. 3 | β-scission mechanism of PO hydrocracking over Ru_1-ZrO_2. **a** Reaction pathways and DFT calculated energy profiles of PP hydrocracking to gas products via β-scission mechanism with carbonium ions (energy unit: eV). The molecule structures in red or blue color are the same type of carbonium circularizing in the hydrocracking loop. **b** Schematic catalytic cycle of PO (PE or PP) hydrocracking on Ru_1-ZrO_2.

3 MPa yields 85 mL of centrifuge-collected liquid (Fig. 4b). The hydrocarbon distribution (Supplementary Fig. 31) is identical to that derived from virgin polyolefins (Fig. 1b), consisting of 70% jet-, 80% gasoline- and 45% diesel-ranged fuels in the liquid (Fig. 4c), and 100% LPG in gas product (containing more than 70% C_3-C_4 hydrocarbons) without forming methane and ethane.

Driven by global initiatives to reduce carbon emissions and stringent environmental regulations, the demand for sustainable aviation fuel is on a rapid rise over the coming years, starting from 2023, with a compound annual growth rate (CAGR) of 45%[47]. The use of centrifugation to obtain 85 mL of liquid containing 70% jet-fuel-ranged hydrocarbons significantly lowers the cost of post-reaction product separation. It demonstrates the potential for scaling up the production of waste plastic-derived sustainable jet fuel. Furthermore, the absence of methane and ethane in the gas products (LPG) allows them to be directly liquified at ambient pressure, making them

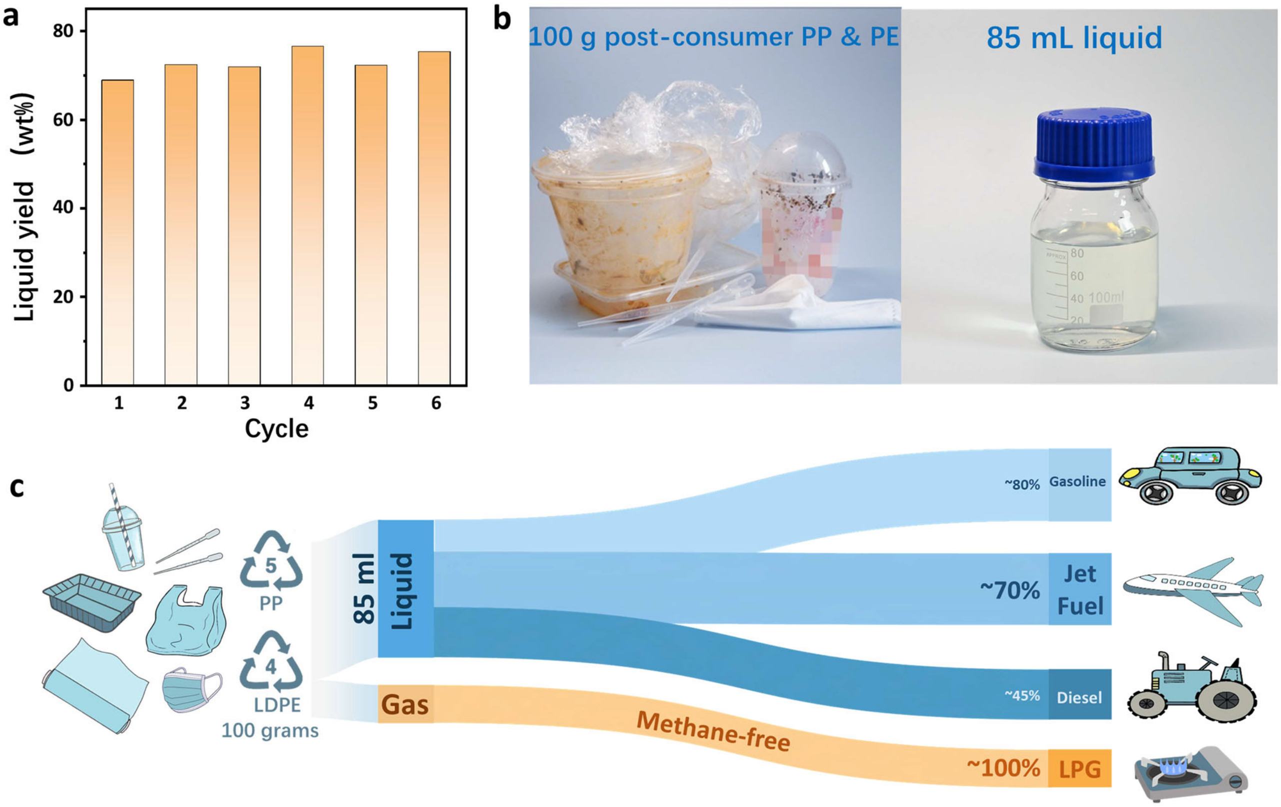

Fig. 4 | Potential of Ru_1-ZrO_2 in practice. a Liquid yields in the cycling experiments on Ru_1-ZrO_2. **b**, **c** Hydrocracking of 100 g post-consumer PP and PE substrates on Ru_1-ZrO_2 at 300 °C under 3 MPa H_2 for 8 hours: photos of the post-consumer plastics and the liquid product (**b**) and product selectivity (**c**).

suitable for use in heating appliances, cooking equipment, and vehicles.

Discussion

The hydrocracking PO waste to liquid fuels not only mitigates plastic pollution but also conserves valuable fossil resources, contributing to the advancement of a circular economy. The use of atomic Ru-doped ZrO_2 marks a paradigm shift in catalyst design, moving from traditional supported-metal manipulation to oxide-based mediation. In this case, the atomic Ru activates its neighboring O atom within the Ru-O-Zr moiety, making it the critical center for selective internal C–C bond cleavage, rather than relying on the Ru site itself. The atomic-level communication between the hydrogenation/dehydrogenation site (metal dopant) and the isomerization/cracking site (neighboring O site) ensures the efficient transfer of PO in between, preventing undesirable hydrogenolysis to methane and ethane at the metal site. Despite ruthenium's well-established role as a methanation catalyst, this oxide modulation strategy demonstrates its potential to prevent methane formation for the ideal hydrocracking of polyolefins to methane-free fuels. Furthermore, the Ru_1-ZrO_2 catalyst has demonstrated its effectiveness in reactions on the hundred-gram scale, offering promising application potential for large-scale chemical upcycling of polyolefin plastics.

Methods

Synthesis of Ru_1-ZrO_2 and Ru_1-ZrO_2_500

Ru_1-ZrO_2 was prepared by the hard-template method. Typically, $Zr(NO_3)_4{\bullet}5H_2O$ and $Ru(NO)(NO_3)_x(OH)_y$ were added to deionized water to form a solution. This solution was added to Carbon black powder which was used as the hard-template. The obtained mixture was dried at 80 °C for 12 hours, and then calcined in air at 500 °C for 6 hours to remove the Carbon black template. Before the hydrocracking reaction, the sample was pretreated in 20% H_2/Ar with a flow rate of 50 mL/min at 275 °C (300 °C was used for pretreatment when the hydrocracking reaction temperature was 300 °C) to obtain Ru_1-ZrO_2. The loading of Ru in Ru_1-ZrO_2 used in this work was determined by ICP (Supplementary Table 3) at 1.3 wt%. The Ru_1-ZrO_2 catalyst was treated in 20% H_2/Ar with a flow rate of 50 ml/min at 500 °C for 0.5 hours to obtain Ru_1-ZrO_2_500. The bare ZrO_2 as the reference was prepared using the same method without loading Ru.

Hydrocracking reaction

In a typical hydrocracking reaction, PP, or PE, normal alkane (C_8 and C_{12}), or squalane (4 g), and the Ru_1-ZrO_2 catalyst (0.4 g) were loaded into a stainless steel autoclave batch reactor (25 mL). The reactor was then flushed with Ar under 0.4 MPa for 8 cycles, followed by 5 cycles of H_2 flush with 0.5 MPa pressure above the target reaction pressure. Afterward, the reactor was pressurized with H_2 to the target pressure (1–4 MPa) at room temperature. Then, the reactor was placed in its associated heater with a temperature controller and heated to target temperatures (250 °C or 300 °C) at a rate of 7.5 °C/min and maintained for target durations (2, 8 hours). Stirring with a rate of 600 rpm was engaged after the temperature reached 160 ± 5 °C. The temperature and pressure were automatically recorded once per minute during the entire reaction. At the end of the reaction, the reactor was cooled to and maintained at 10 °C for 15 minutes to equilibrate the gas and liquid product transformation before the product collection.

The hydrocracking of 100 g of post-consumer PP and PE plastic wastes with 10 g of catalysts was performed in a batch stainless steel autoclave with a volume of 1 L. The post-consumer products, such as lunch boxes, soft drink cups, masks, shopping bags, pipets, and packing films, were picked up from the trash bin and washed before the hydrocracking reaction. The procedure was the same as the mentioned above.

Product collection and analysis

Product collection and calculation. The products were collected and analyzed according to the method depicted in Supplementary Fig. 32. Gas product was charged to a gas sampling bag via the valve-connected tube on the cap of the reactor. The liquid products and insoluble solids, including the catalyst were then collected in a weighted centrifuge tube (M_T), and then weighed and denoted as M_P. The liquid product was collected by centrifuging and stored in a vial for GC analysis later. The separated insoluble solids were kept in the centrifuge tube and then washed with *n*-hexane after drying at 80 °C for 24 hours (the products solved in the wash solution of *n*-hexane were mainly under C_{22} which was identical to that of centrifuging collected liquid. Only trace amounts of hydrocarbons C_{22}-C_{25} was observed). The centrifuge tube with post-washed solids was dried at 80 °C in an oven for 24 hours, aiming to vaporize all the liquid, and then weighed as M_1.

The masses of products in different phases were calculated using the following formulas:

$$M_L = M_P - M_1 \tag{1}$$

$$M_S = M_1 - M_T - M_C \tag{2}$$

$$M_G = M_{Plastic} - M_L - M_S \tag{3}$$

where M_L, M_S, M_G and $M_{Plastic}$ are the mass of liquid product, solid residue, gas product, and plastic substrate, respectively. The M_C is the mass of the catalyst, in most cases in this study it is 0.4 g.

The yield of products (Y_i) and conversion were calculated as follows:

$$Y_i = \frac{M_i}{M_{Plastic}} \times 100\% \tag{4}$$

$$Conversion = \left(1 - \frac{M_S}{M_{Plastic}}\right) \times 100\% \tag{5}$$

where i is L, S, G, representing liquid product, solid residue, and gas product, respectively. Given the mass of the H_2 input and consumption was much less than that of plastic substrates, it was ignored when calculating the conversion of plastics.

Gas product analysis. The gas product collected in the gas bag was analyzed using a GC (Agilent 8890 Series) with a FID detector and a HP-PlOT-Q column. The method was established and calibrated by using a standard gas reference which involved methane of 0.1 mol%, ethane of 0.1 mol%, propane of 0.1 mol%, isobutane of 0.1 mol%, butane of 0.1 mol%, neopentane of 0.1 mol%, isopentane of 0.1 mol% and pentane of 0.1 mol%. A gastight syringe was used to inject 0.3 mL gas sample to quantify the relative ratio of C_1-C_6 hydrocarbons. A typical chromatogram showing the separation of species with retention time is shown in Supplementary Fig. 2.

The mass yield of each component of the gas product can be calculated according to Eq. 6:

$$Y_{G_i} = \frac{A_i}{\sum_1^6 A_i} \times Y_G \tag{6}$$

where Y_{G_i} is the yield of the gas hydrocarbon with the carbon number i; A_i is the chromatographic area of gas hydrocarbon with the carbon number as i; i represents carbon number of 1-6; Y_G is the yield of gas product obtained in equation (4).

Liquid products analysis. They were quantitatively analyzed on an Agilent 8890 gas chromatograph equipped with an Agilent HP-5 capillary column and FID. The inlet and detector temperatures were 300 °C, respectively. Typically, 1 μL of liquid product was injected into the chromatogram using a syringe. The standard *n*-alkanes C_7-C_{40} purchased from Sigma-Aldrich was used to establish the GC method and perform a quantitative analysis. A typical chromatogram for the liquid product and the standard mixture of *n*-alkanes (C_7-C_{40}) obtained from Sigma-Aldrich is shown in Supplementary Fig. 33. The same method was concurrently used for qualitative analysis using GC-MS. (A typical GC-MS result is shown in Supplementary Fig. 34).

The products for hydrocarbons based on carbon number can be calculated according to the following formula:

$$Y_{L_i} = \frac{A_i}{\sum_5^{25} A_i} \times Y_L \tag{7}$$

where Y_{L_i} is the yield of the liquid hydrocarbon with the carbon number i; A_i is the chromatographic area of liquid hydrocarbon with the carbon number as i; i represents carbon number of 5-25; Y_L is the yield of liquid product obtained in equation (4).

Mass balance examination

To calculate the mass balance, the mass yield of gas was measured independently by using the volume of the gas product combined with GC analysis as follows:

The pressure as a function of the gas volume in the reactor at 10 °C was established using a measuring bubbler. Therefore, the post-reaction gas volume can be calculated by using the pressure at the end of the reaction. Combined with the ratio of gaseous species mentioned above, the mass of each species can be calculated independently by using the formula below:

$$M_{G_i} = \frac{\frac{A_i}{k_i} \times W_i \times V_G}{22.4} \tag{8}$$

Where A_i is the chromatographic area of different carbon numbers; k_i represents the correction factor for the respective component, which is established using 0.3 mL injection of standard gas reference mentioned above and shown in Supplementary Fig. 2; W_i is the corresponding relative molecular weight; V_G is the volume of the gas at the end of the reaction.

The mass balance was examined by:

$$mass\ balance = \frac{\sum_1^6 M_{G_i} + M_L + M_S}{M_{Plastic}} \times 100\% \tag{9}$$

Where M_{G_i}, M_L and M_S are the mass of gas, liquid and solid residue. They are all measured independently based on the above methods. Given that the mass of the H_2 input and consumption is much less than that of plastic substrates, it is ignored when calculating the mass balance.

Due to the mass loss of products during the independent collection of gas and liquid products and the error of measurements, particularly for the gas volume, the mass balance cannot meet 100% but all still keep the mismatch within 10%. The result of mass balance is shown in Supplementary Fig. 35.

In situ Pyridine-FTIR characterization

In situ Pyridine-FTIR was conducted in a vacuum cell with a Fourier transform infrared spectrometer ThermoFisher iS50r equipped with an MCT detector. Ru_1-ZrO_2 sample was pressed to a wafer and loaded into the sample holder. Before pyridine adsorption, the Ru_1-ZrO_2 wafer was degassed under vacuum at 150 °C for 20 min and then cooled to room temperature. The background spectra of the samples were acquired in the vacuum before introducing pyridine vapor. The pyridine vapor was introduced into the cell by using a vacuum pump and kept until the intensity of the IR peaks did not increase. Subsequently, the cell was evacuated to remove gas-phase pyridine until the IR peak did not decrease at room temperature and then the wafer was heated to 450 °C to desorb pyridine. After the desorption, the Ru_1-ZrO_2 wafer was reduced at 500 °C for 30 min in 20% H_2/Ar, aiming to in situ obtain Ru_1-ZrO_2_500. After this reduction, the wafer was cooled to room temperature, and the above procedure was repeated for pyridine adsorption/desorption. The ZrO_2 was pressed to the wafer for Py-FTIR characterization as a reference. Due to the difference in transmittance and the weight of ZrO_2 and Ru_1-ZrO_2 wafers in ex-situ measurements, the intensity of the peak at 1444 cm^{-1} was normalized to the spectra of ZrO_2 and Ru_1-ZrO_2 in Fig. 2i.

H_2/D_2 exchange experiment

H_2/D_2 exchange experiment was performed at 250 °C and mass spectrometry was used to record the signal intensities. Typically, 50 mg catalyst was loaded into the reactor and 10% H_2/Ar was introduced with a flow rate of 20 ml/min at 250 °C. After the stabilization of the mass spectrometry signal, the flow of 10% H_2/Ar was switched to the flow of D_2/Ar with a rate of 20 mL/min. The signal of M/Z = 3 (HD) was recorded throughout the process. After the testing of Ru_1-ZrO_2 was completed, the reactor was gradually heated to 500 °C at a rate of 10 °C/min under the atmosphere of 20 ml/min 20% H_2/Ar for in situ reduction for 0.5 hours, aiming to obtain the sample of Ru_1-ZrO_2_500 in situ. Subsequently, the reactor was cooled down to 250 °C to conduct the H_2-D_2 exchange experiment again for Ru_1-ZrO_2_500 catalyst.

Computational details

All DFT calculations were performed using the Vienna Ab Initio Simulation package (VASP 5.4.4)[48,49]. The generalized gradient approximation (GGA) with PBE exchange and correlation functional was used to account for the exchange-correlation energy[49,50]. The kinetic energy cutoff of the plane wave basis set was set to 400 eV. The threshold for energy convergence for each iteration was set to 10^{-5} eV. Geometries were assumed to be converged when forces on each atom were less than 0.05 eV/Å. Gaussian smearing of the population of partial occupancies with a width of 0.05 eV was used during iterative diagonalization of the Kohn-Sham Hamiltonian.

The bulky ZrO_2 unit cell in the tetragonal phase was first fully optimized. The optimized lattice vectors of a = b = 3.612 Å and c = 5.212 Å have a good agreement with the experiment parameters[51]. The most stable (101) surface of ZrO_2 tetragonal phase was simulated by a 3×4×1 supercell slab model including three ZrO_2 sub-layers (each includes two oxygen atomic layers and one Zr atomic layer) separated by a vacuum layer with a thickness of 15 Å along the surface normal direction to avoid spurious interactions between periodic slab models. The bottom two layers of ZrO_2 were fixed, while the rest was allowed to relax during the geometry optimization. One Zr atom on the surface was replaced by Ru to create a Ru-O-Zr moiety. The lattice parameters were fixed throughout the surface calculations. Corrections for on-site Coulomb interactions by use of the DFT + U procedure were done with effective U = 4 eV for Zr. The Brillouin zone integration and k-point sampling were restricted to the gamma point. The nudged-elastic band method with the improved tangent estimate (CI-NEB) was used to determine the minimum energy path and to locate the transition state structure for each elementary reaction step[52]. The transition state was confirmed by observing only one imaginary frequency corresponding to each reaction coordinate.

The alkane of C11 with the branched methyl groups was used as a model compound. The adsorption energy of the reaction intermediate was calculated as $E_{ads} = E_{adsorbate+surface} - E_{adsorbate} - E_{clean-surface}$. The activation energy (E_a) of a chemical reaction was defined as the energy difference between the initial and transition states, while the reaction energy (ΔE) was defined as the energy difference between the initial and final states.

Data availability

All data generated or analyzed during this study are included in this published article (and its supplementary information file). Source data are provided with this paper.

References

1. Geyer, R., Jambeck, J. R. & Law, K. L. Production, use, and fate of all plastics ever made. *Sci. Adv.* **3**, e1700782 (2017).
2. MacArthur, D. E., Waughray, D. & Stuchtey, M. R. The New Plastics Economy Rethinking the future of plastics. *World Econ. Forum 2016*, https://www3.weforum.org/docs/WEF_The_New_Plastics_Economy.pdf.
3. Korley, L. T. J., Epps, T. H., Helms, B. A. & Ryan, A. J. Toward polymer upcycling-adding value and tackling circularity. *Science* **373**, 66–69 (2021).
4. Cao, R. C. et al. Co-upcycling of polyvinyl chloride and polyesters. *Nat. Sustain.* **6**, 1685–1692 (2023).
5. Du, J. J. et al. Efficient solvent- and hydrogen-free upcycling of high-density polyethylene into separable cyclic hydrocarbons. *Nat. Nanotechnol.* **18**, 772–779 (2023).
6. Kots, P. A., Vance, B. C., Quinn, C. M., Wang, C. & Vlachos, D. G. A two-stage strategy for upcycling chlorine-contaminated plastic waste. *Nat. Sustain.* **6**, 1258–1267 (2023).
7. Conk, R. J. et al. Catalytic deconstruction of waste polyethylene with ethylene to form propylene. *Science* **377**, 1561–1566 (2022).
8. Zhang, F. et al. Polyethylene upcycling to long-chain alkylaromatics by tandem hydrogenolysis/aromatization. *Science* **370**, 437–441 (2020).
9. Xu, Z. et al. Chemical upcycling of polyethylene, polypropylene, and mixtures to high-value surfactants. *Science* **381**, 666–671 (2023).
10. Cen, Z. Y. et al. Upcycling of polyethylene to gasoline through a self-supplied hydrogen strategy in a layered self-pillared zeolite. *Nat. Chem.* **16**, 871–880 (2024).
11. Chen, S. J. et al. Ultrasmall amorphous zirconia nanoparticles catalyse polyolefin hydrogenolysis. *Nat. Catal.* **6**, 161–173 (2023).
12. Zhang, W. et al. Low-temperature upcycling of polyolefins into liquid alkanes via tandem cracking-alkylation. *Science* **379**, 807–811 (2023).
13. Li, H. Q. et al. Hydroformylation of pyrolysis oils to aldehydes and alcohols from polyolefin waste. *Science* **381**, 660–665 (2023).
14. Zhang, Z. et al. Recovering waste plastics using shape-selective nano-scale reactors as catalysts. *Nat. Sustain.* **2**, 39–42 (2019).
15. Martín, A. J., Mondelli, C., Jaydev, S. D. & Pérez-Ramírez, J. Catalytic processing of plastic waste on the rise. *Chem* **7**, 1487–1533 (2021).
16. Qiu, Z. T. et al. A reusable, impurity-tolerant and noble metal-free catalyst for hydrocracking of waste polyolefins. *Sci. Adv.* **9**, eadg5332 (2023).
17. Ran, H. S., Zhang, S., Ni, W. Y. & Jing, Y. X. Precise activation of C-C bonds for recycling and upcycling of plastics. *Chem. Sci.* **15**, 795–831 (2024).
18. Liu, S. B., Kots, P. A., Vance, B. C., Danielson, A. & Vlachos, D. G. Plastic waste to fuels by hydrocracking at mild conditions. *Sci. Adv.* **7**, eabf8283 (2021).
19. Tennakoon, A. et al. Catalytic upcycling of high-density polyethylene via a processive mechanism. *Nat. Catal.* **3**, 893–901 (2020).
20. Li, L. et al. Converting plastic wastes to naphtha for closing the plastic loop. *J. Am. Chem. Soc.* **145**, 1847–1854 (2023).
21. Wu, X. et al. Size-controlled nanoparticles embedded in a mesoporous architecture leading to efficient and selective hydrogenolysis of polyolefins. *J. Am. Chem. Soc.* **144**, 5323–5334 (2022).

22. Zhou, Q. M. et al. Mechanistic Understanding of Efficient Polyethylene Hydrocracking over Two-Dimensional Platinum-Anchored Tungsten Trioxide. *Angew. Chem. Int. Ed.* **62**, e202305644 (2023).
23. Vance, B. C. et al. Single pot catalyst strategy to branched products via adhesive isomerization and hydrocracking of polyethylene over platinum tungstated zirconia. *Appl. Catal. B* **299**, 120483 (2021).
24. Wang, M. et al. Complete hydrogenolysis of mixed plastic wastes. *Nat. Chem. Eng.* **1**, 376–384 (2024).
25. Almithn, A. S. & Hibbitts, D. D. Impact of metal and heteroatom identities in the hydrogenolysis of C-X Bonds (X = C, N, O, S, and Cl). *ACS Catal.* **10**, 5086–5100 (2020).
26. Rorrer, J. E., Beckham, G. T. & Román-Leshkov, Y. Conversion of polyolefin waste to liquid alkanes with ru-based catalysts under mild conditions. *JACS Au* **1**, 8–12 (2021).
27. Wang, C. et al. A general strategy and a consolidated mechanism for low-methane hydrogenolysis of polyethylene over ruthenium. *Appl. Catal. B* **319**, 121899 (2022).
28. Jia, C. et al. Deconstruction of high-density polyethylene into liquid hydrocarbon fuels and lubricants by hydrogenolysis over Ru catalyst. *Chem. Catal.* **1**, 437–455 (2021).
29. Vance, B. C. et al. Structure–property relationships for nickel aluminate catalysts in polyethylene hydrogenolysis with low methane selectivity. *JACS Au* **3**, 2156–2165 (2023).
30. Kots, P. A. et al. Electronic modulation of metal-support interactions improves polypropylene hydrogenolysis over ruthenium catalysts. *Nat. Commun.* **13**, 5186 (2022).
31. Chu, M. Y. et al. Site-selective polyolefin hydrogenolysis on atomic ru for methanation suppression and liquid fuel production. *Research* **6**, 0032 (2023).
32. Chen, L. X. et al. Disordered, sub-nanometer Ru Structures on CeO_2 are highly efficient and selective catalysts in polymer upcycling by hydrogenolysis. *ACS Catal.* **12**, 4618–4627 (2022).
33. Nakaji, Y. et al. Low-temperature catalytic upgrading of waste polyolefinic plastics into liquid fuels and waxes. *Appl. Catal. B* **285**, 119805 (2021).
34. Zhang, Z. D. et al. Mixed plastics wastes upcycling with high-stability single-atom Ru catalyst. *J. Am. Chem. Soc.* **145**, 22836–22844 (2023).
35. Wang, C. et al. Polyethylene hydrogenolysis at mild conditions over Ruthenium on Tungstated Zirconia. *JACS Au* **1**, 1422–1434 (2021).
36. Lu, S. L. et al. Enhanced production of liquid alkanes from waste polyethylene via the electronic effect-favored $C_{secondary}$-$C_{secondary}$ bond cleavage. *Chemcatchem* **15**, e202201375 (2023).
37. Weckhuysen, B. M. Creating value from plastic waste. *Science* **370**, 400–401 (2020).
38. Kots, P. A., Vance, B. C. & Vlachos, D. G. Polyolefin plastic waste hydroconversion to fuels, lubricants, and waxes: a comparative study. *React. Chem. Eng.* **7**, 41–54 (2021).
39. Tamura, M. et al. Structure-activity relationship in hydrogenolysis of polyolefins over Ru/support catalysts. *Appl. Catal. B* **318**, 121870 (2022).
40. Liu, J. T. et al. Smart covalent organic networks (CONs) with "on-off-on" light-switchable pores for molecular separation. *Sci. Adv.* **6**, eabb3188 (2020).
41. Zhang, Y. Y. et al. Control of coordinatively unsaturated Zr sites in ZrO_2 for efficient C-H bond activation. *Nat. Commun.* **9**, 3794 (2018).
42. Ftouni, J. et al. ZrO_2 is preferred over TiO_2 as support for the Ru-catalyzed hydrogenation of Levulinic acid to γ-Valerolactone. *ACS Catal.* **6**, 5462–5472 (2016).
43. Sobanska, K., Pietrzyk, P. & Sojka, Z. Generation of reactive oxygen species via electroprotic interaction of H_2O_2 with ZrO_2 Gel: Ionic sponge effect and pH-switchable peroxidase- and catalase-like activity. *ACS Catal.* **7**, 2935–2947 (2017).
44. Maesen, T. L. M., Calero, S., Schenk, M. & Smit, B. Alkane hydrocracking: shape selectivity or kinetics? *J. Catal.* **221**, 241–251 (2004).
45. Girgis, M. J. & Tsao, Y. P. Impact of catalyst metal acid balance in n-hexadecane hydroisomerization and hydrocracking. *Ind. Eng. Chem. Res.* **35**, 386–396 (1996).
46. Souverijns, W., Martens, J. A., Froment, G. F. & Jacobs, P. A. Hydrocracking of isoheptadecanes on Pt/H-ZSM-22: An example of pore mouth catalysis. *J. Catal.* **174**, 177–184 (1998).
47. Sustainable Aviation Fuel Market. *Global Market Insights Inc*, https://www.gminsights.com/industry-analysis/sustainable-aviation-fuel-market (2023).
48. Kresse, G. & Furthmuller, J. Efficiency of ab-initio total energy calculations for metals and semiconductors using a plane-wave basis set. *Comp. Mater. Sci.* **6**, 15–50 (1996).
49. Kresse, G. & Furthmuller, J. Efficient iterative schemes for ab initio total-energy calculations using a plane-wave basis set. *Phys. Rev. B* **54**, 11169–11186 (1996).
50. Perdew, J. P., Burke, K. & Ernzerhof, M. Generalized gradient approximation made simple. *Phys. Rev. Lett.* **77**, 3865–3868 (1996).
51. Igawa, N. & Ishii, Y. Crystal structure of metastable tetragonal zirconia up to 1473 K. *J. Am. Ceram. Soc.* **84**, 1169–1171 (2001).
52. Henkelman, G., Uberuaga, B. P. & Jónsson, H. A climbing image nudged elastic band method for finding saddle points and minimum energy paths. *J. Chem. Phys.* **113**, 9901–9904 (2000).

Acknowledgements

The authors thank Prof. Harry Bitter, Prof. Baoyu Xia, and Dr. János Szanyi for highly fruitful discussions. G.L. acknowledges the Dutch Organization for Scientific Research (NWO) for access to the Dutch national e-infrastructure. This work was supported by the National Natural Science Foundation of China (22472015), Science and Technology Projects of Liaoning (2023JH2/101700290), and the Fundamental Research Funds for the Central Universities (DUT24ZD111).

Author contributions

X.W. conceived the project. J.Y., Z.L., and X.W. performed most of the reactions and characterizations. G.L. conducted the DFT calculation. J.Y., G.L., Z.L., Y.D., R.C., and X.W. analyzed the data. X.Y., J.L., Xiaoru W., and B.W. assisted in the reaction testing. F.T., T.H., X.X., L.H., F.Z., S.Z., Jiong L., and Y.C. provided support for material characterization. J.Y., G.L., and X.W. wrote the paper. All authors contributed to the discussion and revision of the paper.

Competing interests

The authors declare no competing interests.

Additional information

Supplementary information The online version contains supplementary material available at https://doi.org/10.1038/s41467-025-57998-x.

Correspondence and requests for materials should be addressed to Xiang Wang.

Peer review information *Nature Communications* thanks the anonymous reviewers for their contribution to the peer review of this work. A peer review file is available.

Reprints and permissions information is available at http://www.nature.com/reprints